



Cite this: *J. Mater. Chem. A*, 2015, **3**, 3868

Interfacial electron transfer in photoanodes based on phosphorus(v) porphyrin sensitizers co-deposited on SnO₂ with the Ir(III)Cp* water oxidation precatalyst†

Prashanth K. Poddutoori,^a Julianne M. Thomsen,^b Rebecca L. Milot,^b Stafford W. Sheehan,^b Christian F. A. Negre,^b Venkata K. R. Garapati,^a Charles A. Schmittenmaer,^{*b} Victor S. Batista,^{*b} Gary W. Brudvig^{*b} and Art van der Est^{*a}

We introduce phosphorus(v) porphyrins (PPors) as sensitizers of high-potential photoanodes with potentials in the 1.62–1.65 V (vs. NHE) range when codeposited with Ir(III)Cp* on SnO₂. The ability of PPors to advance the oxidation state of the Ir(III)Cp* to Ir(IV)Cp*, as required for catalytic water oxidation, is demonstrated by combining electron paramagnetic resonance (EPR), steady-state fluorescence and time-resolved terahertz spectroscopy (TRTS) measurements, in conjunction with quantum dynamics simulations based on DFT structural models. Contrary to most other types of porphyrins previously analyzed in solar cells, our PPors bind to metal-oxide surfaces through axial coordination, a binding mode that makes them less prone to aggregation. The comparison of covalent binding *via* anchoring groups, such as *m*-hydroxybenzoate ([−]OPh–COO[−]) and 3-(3-phenoxy)-acetylacetonate ([−]OPh–AcAc) as well as by direct deposition upon exchange of a chloride (Cl[−]) ligand provides insight on the effect of the anchoring group on forward and reverse light-induced interfacial electron transfer (IET). TRTS and quantum dynamics simulations reveal efficient photoinduced electron injection, from the PPor to the conduction band of SnO₂, with faster and more efficient IET from directly bound PPor than from anchor-bound PPors. The photocurrents of solar cells, however, are higher for PPor–OPh–COO[−] and PPor–OPh–AcAc than for the directly bound PPor–O[−] for which charge recombination is faster. The high-potentials and the ability to induce redox state transitions of Ir(III)Cp* suggest that PPor/SnO₂ assemblies are promising photoanode components for direct solar water-oxidation devices.

Received 19th December 2014
Accepted 2nd January 2015

DOI: 10.1039/c4ta07018f

www.rsc.org/MaterialsA

1. Introduction

Solar energy research is driven by the need of viable and sustainable alternatives to fossil fuels.^{1–3} One research strategy is to mimic natural photosynthesis by using sunlight for direct production of molecular compounds that could be used as energy carriers.^{4–9} The overall process can be envisioned as a light-driven electrochemical cell in which the anodic reaction extracts electrons from water, releasing protons and oxygen, while the cathodic reaction reduces protons, carbon dioxide, or

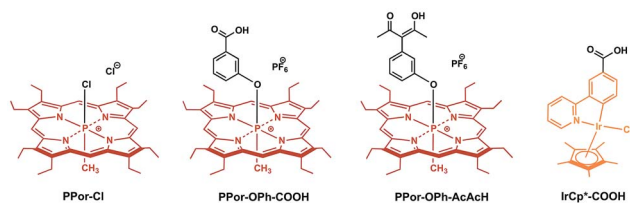
some other species to generate fuel energy carriers. A number of recent studies have explored dye-sensitized metal oxide semiconductors as anodes for such photoelectrochemical cells.^{10–16} Among the challenges in designing such a system is simultaneously achieving a high quantum yield of electron injection into the semiconductor and long-lived charge separation, while generating sufficient oxidizing potential for catalytically withdrawing electrons from water. Two key components of the cell that can be manipulated to optimize performance are the photosensitizer and the linker with which it is attached to the metal oxide.⁹

Porphyrins are widely used as photosensitizers because they are redox-tunable and absorb strongly in the visible light region of the solar spectrum. However, most porphyrins are not sufficiently strong oxidants to function in water-splitting systems, so strongly electron-withdrawing substituents such as pentafluorophenyl functional groups are often needed to raise their redox potentials.^{10,15} An alternative could be phosphorus(v) porphyrins (PPor).^{17–20} The hexavalent

^aDepartment of Chemistry, Brock University, 500 Glenridge Ave., St. Catharines, Ontario, Canada L2S 3A1. E-mail: ppoddutoori@brocku.ca; avde@brocku.ca

^bDepartment of Chemistry, Yale University, P.O. Box 208107, New Haven, CT, 06520-8107, USA. E-mail: charles.schmittenmaer@yale.edu; victorbatista@yale.edu; gary.brudvig@yale.edu

† Electronic supplementary information (ESI) available: Details of experimental methods, synthesis, structural characterization, NMR data, absorption studies, emission spectra, J–V curve, TDDFT calculated absorption spectrum, frontier molecular orbitals and calculated transitions. See DOI: 10.1039/c4ta07018f



Scheme 1 Structures of the investigated PPor photosensitizers and IrCp* water-oxidation precatalyst.

phosphorus center in these porphyrins has a formal oxidation state of +5 and is, thus, extremely electron deficient. As a result, the midpoint potential for oxidation of the porphyrin ring is shifted to much higher values compared to the free-base porphyrin or most metalloporphyrins.^{17,19–23} In addition to its influence on the oxidative potential, the phosphorus center also provides two additional sites for covalently binding substituents, allowing a greater range of possibilities for attaching donors and acceptors.^{17,24,25} These properties suggest that PPors may be good sensitizers in dye-sensitized anodes designed to perform photoinduced water oxidation. Despite these promising features, PPors have been rarely explored towards dye-sensitized solar cells (DSSCs) or photoelectrochemical cells.²⁶ Within the PPor family, the octaethylporphyrin (OEP) derivatives are the best candidates because they can form axial bonds to two different substituents, one on each face of the porphyrin, which makes a greater number of molecular structures for the complexes possible.^{19,27} In addition, the energy of the LUMO lies ~ 0.5 V above the conduction band of SnO₂, providing a reasonable driving force for electron injection without any structural modifications.

Inspired by previous studies of photoanodes with other high-potential porphyrins,^{10,12,15,28} we report on the construction and characterization of PPor-based high-potential photoanodes. Using their axial-bonding capabilities, we have covalently linked PPor to SnO₂ using carboxylate, or acetylacetonate anchoring groups, or by direct deposition upon Cl[−] exchange (Scheme 1). The selected anchoring groups enable us to evaluate the electron-injection properties of the porphyrins as a function of the attachment motif, using various spectroscopic and photoelectrochemical methods and quantum dynamics simulations.

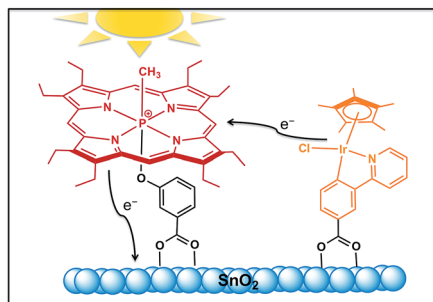


Fig. 1 Proposed mechanism for photooxidation of iridium water-splitting precatalyst (IrCp*) by PPor on SnO₂ surface.

In addition, we examine the ability of PPor-OPh-COOH to activate the water-oxidation pre-catalyst IrCp*,^{29–31} co-deposited on the semiconductor surface (Fig. 1) to avoid the synthetic challenges of connecting the catalyst covalently to the photosensitizer.^{32,33} We find spectroscopic evidence of electron injection from the photo-excited PPor into the conduction band of SnO₂, followed by secondary electron transfer from IrCp* to the oxidized porphyrin. The ability of the molecular assembly to photooxidize IrCp* suggests that it may be possible to construct photoanodes for water oxidation based on this design principle.

2. Experimental section

2.1 Synthesis

Details of the synthesis of the compounds shown in Scheme 1 can be found in the ESI.† Because of its reactivity towards protic solvents, freshly prepared crude PPor-Cl was used in the preparation of PPor-OPh-COOH, PPor-OPh-AcAcH, and PPor-OR (reactions (ii), (iii) and (iv) in Scheme S1†). For the surface binding and spectroscopic studies, PPor-Cl was purified by dry hexane washing to remove 2,6-lutidine and unreacted OEP. The purified compound was stored under inert atmosphere to prevent hydrolysis of the P-Cl bond. The compounds PPor-OPh-COOH and PPor-OPh-AcAcH were prepared from PPor-Cl by reaction with 3-hydroxybenzoic acid and 3-(3-hydroxy)acetylacetone, respectively, under dry, inert conditions at room temperature as shown in Scheme S1.†

2.2 Preparation of thin films of dye-sensitized SnO₂

Dye-sensitized thin films for construction of solar cells and for photocurrent studies were prepared by using previously published methods.¹⁰ Briefly, SnO₂ nanoparticles (NanoArc, average particle size: 33 nm, specific surface area: 30 m² g^{−1}) were mixed into a paste by combining 1.1 g of dry nanoparticles with 2 mL of de-ionized water. The paste was then doctor-bladed onto a fluorine-doped tin(IV)oxide (FTO)-coated glass slide using 0.5 cm × 0.5 cm and 1 cm × 1 cm templates for solar cells and photocurrent studies, respectively, yielding a film ~ 10 μm thick. The resulting films were then sintered in air at 450 °C for two hours and sensitized with the reference photosensitizer N719 or with one of the porphyrin dyes (PPor-OPh-COOH, PPor-OPh-AcAcH or PPor-Cl) by soaking for 12 h in a 0.1 mM solution of the dye in ethanol or dichloromethane, respectively. The films were then dried at room temperature before use. The same preparation procedure was used for diffuse reflectance UV-visible and THz studies except that films were deposited onto 1 mm thick fused silica microscope slides (1 × 1 in, GM Associates) instead of FTO-coated glass.

2.3 Dye-sensitized solar cell (DSSC) assembly and testing

DSSCs were assembled and tested using previously published guidelines.⁵⁴ Solar cells were constructed using the porphyrin-coated SnO₂ thin films described above as the

anode. The counter electrode was prepared by coating an FTO/glass slide with two drops of 0.01 M H_2PtCl_6 in ethanol and then heating in air at 400 °C for 15 minutes. An electrolyte solution based on the I_3^-/I^- redox couple was prepared, using 0.6 M *tert*-butylammonium iodide, 0.1 M lithium iodide, 0.05 M iodine, and 0.5 M *tert*-butyl pyridine in a 50/50 (v/v) valeronitrile–acetonitrile mixture. DSSCs were assembled with a 60 μm spacer (SX1170-60, Solaronix SA, Switzerland) to sandwich the electrolyte between the electrodes. Cells were then held together by binder clips. Solar cell testing was conducted using a 300 W ozone-free xenon lamp with an AM 1.5 G filter (Newport Corporation) adjusted to 1-sun intensity (100 mW cm^{-2}). Photocurrent–voltage scans were taken using a Keithley 2400 source meter and an average of two or three data sets was taken for each sample. The variation in the photocurrent density and voltage between the data sets was found to be $\sim 0.1 \text{ mA cm}^{-2}$ and $\sim 0.01 \text{ V}$, respectively. Exact surface areas of the working electrodes were determined using a 1200 dpi scanner to accurately determine the current density in mA cm^{-2} .

2.4 Time-resolved THz spectroscopy (TRTS)

TRTS measurements were performed with an amplified Ti:Sapphire laser (Mai Tai SP/Empower-30/Spitfire Ace from Spectra Physics) that produced 4 W of pulsed near-IR light at a 1 kHz repetition rate with a $\sim 35 \text{ fs}$ pulse width and 800 nm center wavelength. Roughly one-quarter of the power was frequency doubled and then filtered to produce 40 mW of 400 nm (3.10 eV) light for the pump beam. Another quarter of the near-IR light was used to generate and detect THz radiation. Terahertz radiation was generated using optical rectification in a ZnTe(110) crystal and detected using free space electro-optic sampling in a second ZnTe(110) crystal. Terahertz data were taken at room temperature, and the average of two or three samples was taken for each data set. To analyze electron injection dynamics, the change in peak time-domain THz transmission was monitored as the time delay between the 400 nm pump pulse and the THz probe pulse was varied. Further information on the spectrometer and technique has been reported in the literature.^{34–36}

2.5 Computational modeling

Quantum dynamics simulations of the interfacial electron transfer (IET) between PPor and SnO_2 were performed as described in earlier work.³⁷ Briefly, the electronic structure was described by the tight-binding Extended Hückel (EH) Hamiltonian. Sn orbital parameters were adjusted to give the appropriate band gap (3.60 eV) for bulk rutile SnO_2 , as reported in the literature.³⁸ The ionization energy of the “p” orbitals was adjusted to ensure injection from excited states involved in the Soret transition of the porphyrin. The ground state electronic structure of the system was obtained after solving the time-independent Schrödinger equation in the Slater atomic orbital's basis set ($|\chi_i\rangle$),

$$H\mathbf{Q}^i = E_q\mathbf{S}\mathbf{Q}^i$$

where \mathbf{H} is the EH Hamiltonian and \mathbf{S} is the overlap matrix. \mathbf{Q} and E_q are the eigenvectors and eigenvalues of the q^{th} molecular orbital $|q\rangle = \sum_i Q_i |\chi_i\rangle$, respectively. The initial state was expanded as a linear combination of molecular orbitals:

$$|\psi_0\rangle = \sum_q C_q |q\rangle = \sum_{q,i} C_q Q_i^q |\chi_i\rangle$$

The propagation of the initial state was performed as follows:

$$|\psi(t)\rangle = e^{-\left(\frac{i}{\hbar} H t\right)} |\psi_0\rangle = \sum_i B_i(t) |\chi_i\rangle$$

where

$$B_i(t) = \sum_{i,q} C_q Q_i^q e^{-\frac{i}{\hbar} E_q t}$$

An integration time step of 1 fs was used for all calculations. To obtain the survival probability, the time dependent wave function was projected onto the atomic orbitals of the sensitizer,

$$P(t) = \sum_i^{\text{sens.}} \sum_j^{\text{all}} B_i^*(t) B_j(t) S_{ij}$$

where the i summation is over the atomic orbitals of the sensitizer, and the summation over j is over the complete basis set. $P(t)$ is the probability that the excited electron remains in an orbital of the sensitizer molecule at time t .

The IET simulation included a $2.50 \times 2.27 \text{ nm}$ slab of SnO_2 rutile (110) surface, including 3 layers of Sn(IV) ions with periodic boundary conditions (PBC). The cell dimension was extended to 50 Å in the [110] direction to include a vacuum spacer (ESI, Fig. S16†).

As a first optimization step, the free porphyrins were optimized separately at the density functional theory (B3LYP/6-31G) level of theory. All these geometry optimizations were performed with GAUSSIAN 09.³⁹ Optimized porphyrin structures were covalently attached to the SnO_2 slab and further optimization at the density functional theory (DFT) level, including the whole PPor/ SnO_2 system, was performed with periodic boundary conditions by using SIESTA.⁴⁰ Only the gamma point was used during the optimization and the GGA/PBE exchange correlation functional with a 200 Ry energy cut-off was employed. Optimization was done with a force tolerance of 0.04 eV Å⁻¹, fixing the two bottom rows of SnO_2 . While computationally demanding, this procedure leads to highly reliable geometries.

2.6 Electron paramagnetic resonance spectroscopy

EPR spectra were recorded using a Bruker Elexsys E580 pulse spectrometer operating in CW mode. EPR samples were prepared by mixing the corresponding molecular components in the presence of SnO_2 nanoparticles in dichloromethane. The three-component system (PPor–OPh–COO[−] + IrCp*–COO[−])/ SnO_2 was prepared as follows. The sensitizer PPor–OPh–COOH

(1.2 μmol), the pre-catalyst $\text{IrCp}^*\text{-COOH}$ (1.2 μmol) and the substrate SnO_2 (0.2 mmol) were added to 1 mL of dichloromethane. The resulting suspension was stirred at room temperature for 12 h. The solvent was evaporated and the sample was dried under a gentle flow of nitrogen gas. The obtained powder was placed in a suprasil EPR sample tube (4 mm o.d.), which was then sealed under vacuum. Two-component conjugates of either the sensitizer or the pre-catalyst bound to SnO_2 were prepared in an analogous manner and used as control samples. The sealed EPR sample tubes were then transferred into the resonator and cooled to 80 K under low light. Spectra were recorded while irradiating the sample with white light from a 150 W lamp.

2.7 Photocurrent measurements

Three-electrode photocurrent measurements were performed using an H-cell configuration with the applied potential held at the open-circuit potential of the cell in the dark, measured as 0.3 V vs. Ag/AgCl . Dye sensitized thin films deposited on conductive FTO-coated glass were used as working electrodes. For the $(\text{PPor-OPh-COO}^- + \text{IrCp}^*\text{-COO}^-)/\text{SnO}_2$ photoanode, the thin film was prepared from a solution containing 0.1 mM PPor-OPh-COOH and 0.025 mM $\text{IrCp}^*\text{-COOH}$. All other control photoanodes were prepared using 0.1 mM solutions of the compound being deposited on the surface. Platinum wire and Ag/AgCl electrodes were used as counter and reference electrodes, respectively. The photocurrent was measured with the electrodes immersed in 0.1 M aqueous Na_2SO_4 under illumination with a $\sim 200 \text{ mW cm}^{-2}$ white-light source coupled to a 400 nm long-pass filter. No additional corrections were made for resistance.

3. Results and discussions

3.1 Characterization of the porphyrin dyes

The structural characterization of the porphyrins using HR-FAB mass spectrometry and NMR (^1H , ^1H - ^1H COSY, ^{31}P , ^{13}C and ^1H - ^{13}C HSQC) spectroscopy confirms that the compounds are phosphorus(v) porphyrins with Ph-COOH and Ph-AcAcH as axial ligands. Based on the NMR integrations, the enol and keto forms of PPor-OPh-AcAcH are present in a ratio 80 : 20% in CD_3CN under our experimental conditions. The details of the structural characterization are given in the ESI.[†]

To construct an approximate energy level diagram of the states involved in possible electron-transfer processes, cyclic voltammograms, absorption spectra and emission spectra of the porphyrins were measured. The results of these measurements are summarized in Table 1 and the raw data are presented in the ESI.[†] The potentials for oxidation and reduction of PPor-OPh-COOH and PPor-OPh-AcAc show only minor shifts compared to the reference compound (PPor-OMe), which suggests that the ground state interaction between the axial aromatic unit and porphyrin is very weak or insignificant.

For PPor , the potential for oxidation of the ground state is 1.62 V vs. NHE. The blue edge of the fluorescence spectra (ESI, Fig. S14[†]) at 594.5 nm places the lowest excited singlet state 2.09 eV above the ground state at a potential of -0.47 V vs. NHE. The maximum at 752 nm in the phosphorescence spectrum of the reference compound PPor-OMe at 77 K (ESI, Fig. S15[†]) yields an energy of 1.65 eV above the ground state at -0.03 V vs. NHE for the lowest excited triplet state. In the absorption spectrum, the Soret band at 418 nm (2.97 eV) corresponds to the energy gap between the ground state and the second excited singlet state of PPor . Using the singlet and triplet energies as well as band edge energy of the SnO_2 conduction band (~ 0.05 V vs. NHE), the energy level diagram shown in Fig. 2 is obtained. From this diagram, it is evident that the porphyrin is well poised to inject

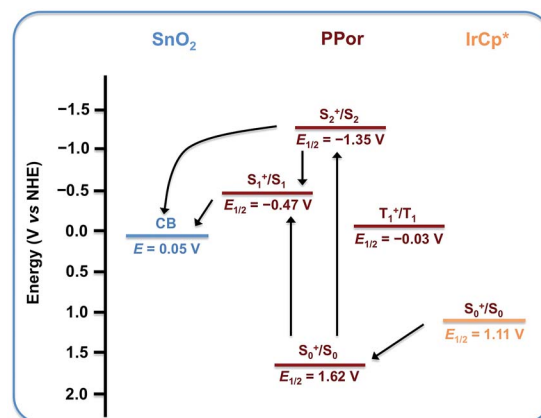


Fig. 2 Energy level diagram of the photo- and redox-active units (PPor , IrCp^* and SnO_2). Note here CB is the conduction band.

Table 1 Redox potentials (vs. NHE), UV-visible absorption and steady-state fluorescence data of investigated compounds in acetonitrile

| Sample | Potential (vs. NHE) ^a | | Absorption λ_{max} , nm (log ϵ) | | Axial ligand ^b / IrCp^* | Fluorescence ^c λ_{max} , nm |
|-----------------------------|----------------------------------|----------------|--|------------------------|---|--|
| | Oxidation | Reduction | B-Band | Q-Band | | |
| PPor-OPh-COOH | 1.62 | $-0.58, -1.03$ | 358 (4.26), 418 (5.27) | 548 (4.01), 590 (4.00) | 290 (3.67) | 600, 654 |
| PPor-OPh-AcAcH | 1.65 | $-0.52, -1.00$ | 358 (4.40), 418 (5.35) | 548 (4.11), 590 (4.10) | 280 (4.06) | 600, 654 |
| PPor-OMe | 1.63 | $-0.56, -1.01$ | 353 (4.41), 416 (5.37) | 548 (4.08), 590 (4.11) | — | 600, 652 |
| PPor-Cl | — | — | 357 (4.25), 415 (5.29) | 546 (3.99), 588 (4.02) | — | — |
| $\text{IrCp}^*\text{-COOH}$ | 1.11, 1.69 | — | — | — | 364 (4.69), 296 (5.20), 255 (5.47) | — |

^a Redox potential measured with 0.1 M TBAPF₆ supporting electrolyte. ^b Unbound ligands 3-(3-hydroxyphenyl)-acetylacetone and 3-hydroxybenzoic acid have absorbance [λ_{max} , nm (log ϵ)] at 281 (3.98) and 296 (3.42), respectively. ^c Excitation wavelength at 550 nm.

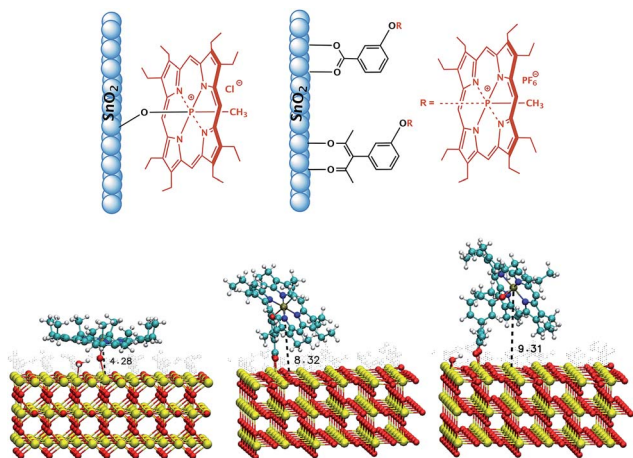


Fig. 3 Schematic representations (top) and DFT optimized structures (bottom) of directly bound and through-anchor bound PPors on SnO_2 surface.

electrons into the conduction band and to extract electrons from $\text{IrCp}^*\text{-COOH}$.

3.2 PPor surface binding studies

PPor-Cl, PPor-OPh-COOH and PPor-OPh-AcAcH were bound to the surface of solid SnO_2 nanoparticles as described in the Experimental section. In the case of PPor-Cl, reaction of the P-Cl bond with active OH groups on the surface of SnO_2 is possible leading to direct covalent binding of the porphyrin (Fig. 3, top left). For PPor-OPh-COOH and PPor-OPh-AcAcH, coordination bonds can be formed by displacement of OH groups on the surface by the carboxylate or AcAc groups of the anchors (Fig. 3, top right).

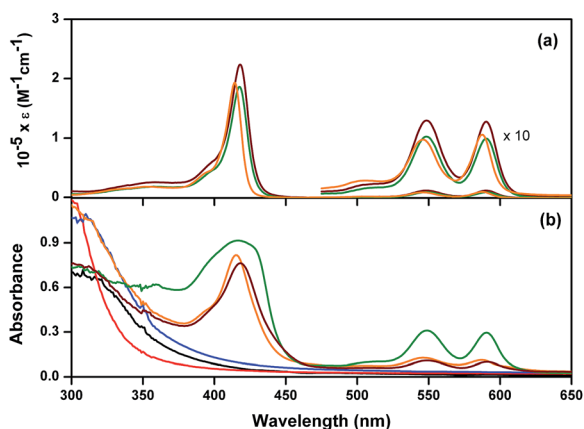


Fig. 4 UV-visible absorption spectra of the newly investigated PPors and their corresponding anchors: (a) in dichloromethane solution and (b) bound to the surface of solid SnO_2 . SnO_2 (black), Ph-AcAcH (blue), Ph-COOH (red), PPor-OPh-AcAcH (maroon), PPor-OPh-COOH (green) and PPor-Cl (orange). The region between 475 nm and 650 nm in the solution spectra is also shown with the absorbance multiplied by a factor of 10 to show the structure of the Q-bands. The spectra of the solid samples were measured by diffuse reflectance methods as described in the ESI.†

UV-visible absorption spectra of surface-bound PPor films are shown in Fig. 4b along with control spectra of the bare surface and the anchoring groups bound to the surface without porphyrin. The corresponding spectra of the PPors in solution are shown in Fig. 4a. Bare SnO_2 (Fig. 4b, black spectrum) as well as Ph-AcAc or Ph-COO⁻ bound to SnO_2 (blue and red spectra, respectively) all only show absorption below 400 nm, due to promotion of electrons into the SnO_2 conduction band. When the PPors are bound to the surface, the Soret band at ~ 420 nm and Q-bands at 550 and 590 nm are also observed (Fig. 4b, green, orange and maroon spectra). The positions of the porphyrin bands are the same as observed in solution (compare Fig. 4a), but broadening of the Soret band is observed. This suggests that the electronic structure of PPor is perturbed weakly by the binding. In general, absorption peak broadening of surface bound porphyrins is a result of overlap of porphyrin molecular orbitals with either the metal oxide surface or other porphyrin molecules.^{41,42} This is possible under two circumstances: (i) close packing or aggregation of porphyrin molecules, and (ii) close proximity between the surface and the porphyrin plane. The spectra in Fig. 4b show that the broadening is roughly the same for both PPor-OPh-AcAc and PPor-O⁻, (maroon and orange spectra), which indicates that it does not depend on the nature of the binding to the surface. On the other hand, for PPor-OPh-COO⁻ both the amount of broadening and the absorbance is greater. Hence, the broadening increases as the amount of porphyrin bound to the surface increases. Together, the lack of dependence on the anchoring group and the dependence on porphyrin concentration indicate that the broadening is due to interactions between the porphyrin molecules and not between the porphyrin and the surface.⁴³

Because the samples were all prepared under the same conditions, the absorbance is also a measure of the relative binding efficiency of the porphyrins. The concentration of porphyrin in the PPor-OPh-COO⁻/ SnO_2 sample is approximately a factor of two higher than in the PPor-OPh-AcAc/ SnO_2 sample suggesting that the COO⁻ group is a better anchoring group than AcAc. This difference may be due to instability of the AcAc anchor in the presence of the metal oxide.¹⁵

3.3 Computational models

Quantum dynamics simulations were performed to explore the photo-injection time scale and the kinetics of IET as influenced by the adsorbate binding modes of PPors bound to SnO_2 , as shown in Fig. 3 (bottom panel). In both PPor-OPh-AcAc (Fig. 3 bottom right) and PPor-OPh-COO⁻ (Fig. 3 bottom middle), the optimized structures show that the plane of the porphyrin is tilted with respect to the SnO_2 surface due to binding of the anchoring groups to the porphyrin *via* the *meta* position of the phenyl group. The tilt angle (measured as the angle between a vector normal to the porphyrin plane and the axis through the anchoring group, see ESI, Fig. S17†) is 57° and 71° for PPor-OPh-AcAc and PPor-OPh-COO⁻, respectively. This tilted orientation forces

one edge of the porphyrin ring into direct contact with the SnO_2 surface, inducing rotation of the ethyl substituent groups away from the surface upon optimization. Adsorption of PPor-O^- , also induces rearrangement of the N-P-O-C dihedral angle to avoid steric interactions with the surface. In the case of directly bound PPor (Fig. 3 bottom left), all of the ethyl groups of PPor were rotated away from the SnO_2 surface leading to an optimized structure in which the plane of the porphyrin ring is nearly parallel to the SnO_2 surface and which is partially stabilized by hydrogen bonding between the O atom of P-O-Sn and a neighboring H_2O molecule. The optimized DFT structures indicate that the center of the porphyrin plane in PPor-O^- and $\text{PPor-O}^-/\text{SnO}_2$ is at 8.32 Å and 9.31 Å away from SnO_2 surface, respectively. In the directly bound system, however, a much shorter distance (4.28 Å) is predicted. The binding modes considered here were constructed in order to avoid a direct contact of the porphyrin ring with the SnO_2 surface. Although we cannot rule out the existence of other binding modes, an exhaustive exploration of all possible modes would be computationally unaffordable due to the size of the present systems.

The molecular orbitals of the system obtained with the optimized geometries were analyzed to find those that participate in the Soret ($S_0 \rightarrow S_2$) transition. Time dependent density functional theory (TDDFT) calculations show the Soret band to be composed of H-n to L and H-n to L + 1 type of transitions, see ESI, Fig. S18 & Table S1.† We have analyzed injection simulations from the L orbital as we verified that L and L + 1 are degenerate and have the same symmetry, both with DFT and EH level of theory (ESI, Fig. S19†). Fig. 5 shows the probability of the electron residing in the adsorbate after photoexcitation to the L and L + 1 orbitals, as a function of time. The calculations predict lifetimes of 0.2, 6.7 and 279 ps for $\text{PPor-O}^-/\text{SnO}_2$, $\text{PPor-O}^-/\text{SnO}_2$ and $\text{PPor-O}^-/\text{SnO}_2$, respectively, for injection into the SnO_2 conduction band. Two conclusions can be drawn from the calculated lifetimes: (i) injection of electrons from the S_2 state of PPor into the conduction band of SnO_2 is effective, and (ii) the injection rates depend on the distance between the donor PPor and the SnO_2 surface.

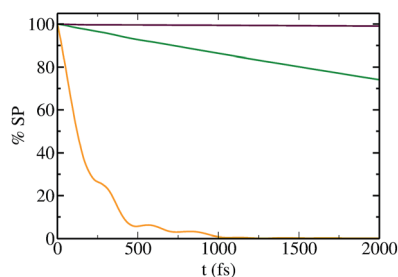


Fig. 5 Dynamic simulation of electron injection in $\text{PPor-O}^-/\text{SnO}_2$ (maroon), $\text{PPor-O}^-/\text{SnO}_2$ (green) and $\text{PPor-O}^-/\text{SnO}_2$ (orange). % SP is the percent survival probability as a function of time.

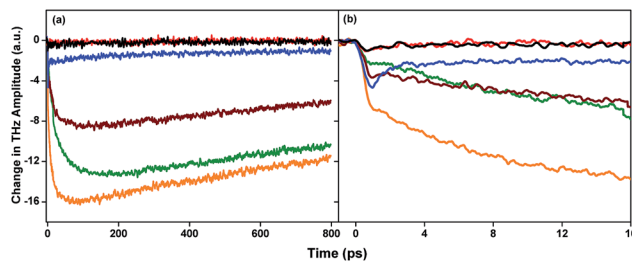


Fig. 6 TRTS electron injection profiles measured to (a) 800 ps and (b) 15 ps following 400 nm photoexcitation of bare SnO_2 (black), $\text{Ph-AcAc}/\text{SnO}_2$ (blue), $\text{Ph-COO}^-/\text{SnO}_2$ (red), $\text{PPor-O}^-/\text{SnO}_2$ (maroon), $\text{PPor-O}^-/\text{SnO}_2$ (green) and $\text{PPor-O}^-/\text{SnO}_2$ (orange).

3.4 Time-resolved THz spectroscopy (TRTS)

Experimentally, the electron injection efficiency and dynamics can be determined by using time-resolved THz spectroscopy (TRTS). The observed change in THz transmission following pulsed light excitation is proportional to the change in the charge carrier density times the mobility in the conduction band^{36,44} and an increase in the density of mobile charge carriers results in lower THz transmission. Fig. 6 shows the transmission changes, following 400 nm excitation of the dye-sensitized SnO_2 nanoparticles. As controls, we have also measured the electron injection for bare SnO_2 , Ph-COO^- , and Ph-AcAc . Although the injection observed for bare SnO_2 and $\text{Ph-COO}^-/\text{SnO}_2$ was negligible, a measurable amount of injection occurring on a ~ 300 fs time-scale was observed for $\text{Ph-AcAc}/\text{SnO}_2$. Adding the porphyrins greatly increased electron injection efficiency, suggests that the majority of the carriers originate in the porphyrin. The influence of Ph-AcAc injection on the overall injection efficiency of $\text{PPor-O}^-/\text{SnO}_2$ is highlighted in Fig. 6b, which shows the first 15 ps of electron injection. After 1–2 ps, the electron injection from $\text{PPor-O}^-/\text{SnO}_2$ is more efficient than from $\text{PPor-O}^-/\text{SnO}_2$. At about 3 ps, however, $\text{PPor-O}^-/\text{SnO}_2$ overtakes $\text{PPor-O}^-/\text{SnO}_2$ and remains the more efficient injector out to 800 ps. The total amplitude of the TRTS signal for $\text{PPor-O}^-/\text{SnO}_2$ is roughly a factor of two larger than for $\text{PPor-O}^-/\text{SnO}_2$ (Fig. 6). This difference correlates well with the roughly two times higher concentration of PPor-O^- on the SnO_2 surface (Fig. 4). Thus, the relative electron injection efficiency of $\text{PPor-O}^-/\text{SnO}_2$ and $\text{PPor-O}^-/\text{SnO}_2$ is about the same. In contrast, the amplitude of the TRTS signal from the PPor-O^- sample is more than twice that of the $\text{PPor-O}^-/\text{SnO}_2$ sample even though the two samples have the same absorbance. Hence, PPor-O^- has a higher electron injection efficiency, as would be expected due to the shorter distance between the porphyrin and the surface.

The kinetics of the electron injection from $\text{PPor-O}^-/\text{SnO}_2$, $\text{PPor-O}^-/\text{SnO}_2$ and $\text{PPor-O}^-/\text{SnO}_2$ were quantified by fitting eqn (1) to the measured data, using the Levenberg–Marquardt nonlinear least-squares fitting algorithm.

$$\Delta\text{THz} = \Delta\text{THz}_0[A_1(e^{-t/\tau_1} - 1) + A_2(e^{-t/\tau_2} - 1) + (1 - e^{-t/\tau_3})] \quad (1)$$

Electron injection is modeled as a double exponential with time constants τ_1 and τ_2 and corresponding relative amplitudes A_1 and A_2 (where $A_1 + A_2 = 1$) to account for electron injection from the second excited singlet state (S_2) and first excited singlet state (S_1) of the porphyrin, respectively;^{28,45} ΔTHz is the measured change in TRTS amplitude as a function of pump/probe delay time, and ΔTHz_0 is the maximum change in TRTS amplitude. The $1 - e^{-t/\tau_r}$ term accounts for recombination. Before fitting the PPor-OPh-AcAc data, the signal contribution due to injection from the Ph-AcAc anchor was removed by subtracting the Ph-AcAc control experiment trace from the PPor-OPh-AcAc trace. A global fit was performed in which τ_r was a shared parameter because loss of mobility over this short time scale is most likely due to trapping in the SnO_2 nanoparticles and not due to sensitizer cation reduction. The results of the fit are summarized in Table 2.

The lifetimes for electron injection by PPor-OPh-COO⁻ and PPor-OPh-AcAc are roughly 3 ps and 30 ps for both sensitizers, and these values are similar to those reported for free-base and pentafluorophenylzinc(II) porphyrin bound to SnO_2 nanoparticles.²⁸ Possible pathways for the injection can be determined by considering the energies and lifetimes of the excited states. As shown in Fig. 2, the lower edge of the conduction band is 1.4 eV and 0.52 eV lower in energy than the S_2 and S_1 states of PPor, respectively. Thus, there is adequate driving force for electron injection from both of these states. In solution, the lifetimes of the S_2 and S_1 states of PPors have been reported as 1.5 ps and 4.8 ns, respectively.^{19,45} The observed values of the electron injection lifetime τ_1 are similar to the reported lifetime of the S_2 state, while the τ_2 values are about an order of magnitude longer than the S_2 lifetime but two orders of magnitude shorter than the S_1 lifetime. Thus, τ_1 is consistent with injection from the S_2 state and appears to be limited by the lifetime of the state. We assign τ_2 to injection from S_1 , which is fast compared to other decay processes for S_1 . Although the lowest excited triplet state is slightly higher in energy than the conduction band edge, injection from the triplet state can be ruled out because the kinetics show that injection is much faster than intersystem crossing.

Compared to PPor-OPh-COO⁻ and PPor-OPh-AcAc, electron injection is much faster for PPor-O⁻. This result is consistent with other studies that observe increased electron-transfer rates with decreased linker length.^{46–48} Additionally, A_1 , which is the fraction of injected electrons associated with τ_1 , is

Table 2 TRTS curve fitting parameters of investigated PPor on SnO_2 surface. Change in terahertz amplitude (ΔTHz_0), injection lifetimes (τ_1 and τ_2), their corresponding amplitudes (A_1 and A_2), and trapping lifetime (τ_r)

| Sample | ΔTHz_0 | A_1 | τ_1 (ps) | A_2 | τ_2 (ps) | τ_r^a (ps) |
|---------------------------|----------------------|-------|---------------|-------|---------------|-----------------|
| PPor-OPh-COO ⁻ | 14.5 | 0.19 | 2.13 | 0.81 | 35.9 | 2354 |
| PPor-OPh-AcAc | 7.8 | 0.33 | 4.05 | 0.67 | 28.9 | 2354 |
| PPor-O ⁻ | 16.5 | 0.41 | 0.55 | 0.59 | 12.4 | 2354 |

^a This parameter was shared across all three data sets in the global fitting procedure.

larger for PPor-O⁻ than for PPor-OPh-COO⁻ and PPor-OPh-AcAc. With faster electron injection, competition with deactivation of the S_2 state is decreased, allowing for a larger fraction of electrons to be injected from the higher energy excited state.

Overall, the experimental injection lifetimes (τ_1) are in qualitative agreement with the trends obtained from the injection dynamics calculations. As would be expected, the calculations and experimental data show that the rate of injection from S_2 decreases as the distance between the porphyrin and the SnO_2 slab is increased. For the PPor-OPh-COO⁻ system, the calculated injection curve has a lifetime of 6.7 ps compared to $\tau_1 = 2.13$ ps from the TRTS data. For the PPor-OPh-AcAc system, the simulation gives a lifetime that is considerably larger (279 ps) than the measured value of $\tau_1 = 4.05$ ps, but the observation that the value of τ_1 is longer for PPor-OPh-AcAc than for PPor-OPh-COO⁻ is correctly reproduced. PPor-O⁻ in turn shows an ultra fast injection both with TRTS (0.5 ps) and simulations (0.2 ps). Together, the TRTS spectroscopy and injection simulations show that the presence of the linker slows down the injection from the porphyrin, and slower injection is obtained when the center of the porphyrin is moved away from the surface.

3.5 Solar cell studies

DSSC studies were performed to investigate the photophysical properties of the porphyrins in a working device. Importantly, we are not studying these devices to develop practical solar cells but rather to better understand charge transfer processes. In agreement with our injection studies, we found that the anchor-bound porphyrins are functional sensitizers when incorporated into DSSCs based on SnO_2 photoanodes (ESI, Fig. S20†). Table 3 summarizes the solar cell parameters of the investigated PPors. The devices performed similarly to each other (0.074% and 0.081% for PPor-OPh-COO⁻ and PPor-OPh-AcAc, respectively), yet more poorly than the standard sensitizer N719 (0.76%, see ESI, Fig. S21†). The solar cell performance can be attributed to a number of factors, including the lack of directionality in charge injection compared to N719, low surface coverage due to the large footprint of the axially bound porphyrins, and less coverage of the solar spectrum when compared to ruthenium-based sensitizers. However, the devices allowed us to gain mechanistic insight into the behavior of porphyrins, and to

Table 3 Solar cell parameters, short-circuit current density (J_{sc}), open circuit voltage (V_{oc}), fill factor (FF), and cell efficiency (η) of investigated PPor derivatives on SnO_2 surface with I_3^-/I^- redox couple under 100 mW cm^{-2} AM 1.5 G irradiation

| Sample | J_{sc} (mA cm^{-2}) | V_{oc} (V) | FF ^a | η^b |
|---------------------------|----------------------------------|--------------|-----------------|----------|
| PPor-OPh-COO ⁻ | 0.74 | 0.22 | 0.45 | 0.074 |
| PPor-OPh-AcAc | 0.72 | 0.26 | 0.43 | 0.081 |
| PPor-O ⁻ | 0.16 | 0.13 | 0.38 | 0.008 |
| N719 | 4.80 | 0.41 | 0.39 | 0.76 |

^a $\text{FF} = (J_{mp} \times V_{mp}) / (J_{sc} \times V_{oc})$, where J_{mp} and V_{mp} are maximum power points. ^b $\eta = (\text{power}_{out}) / (\text{power}_{in}) = (V_{oc} \times J_{sc} \times \text{FF}) / (\text{power}_{in})$, where $\text{power}_{in} = 100 \text{ mW cm}^{-2}$.

explore the effect of different anchoring methods on charge recombination in working photoelectrochemical cells.

We found that the anchor-bound porphyrin performed better in solar cell devices than porphyrins bound directly to the oxide surface (ESI, Fig. S20† & Table 3). While directly bound porphyrins inject electrons into SnO_2 much faster than anchor-bound porphyrins, they do not prevent charge carriers from being transferred back into the porphyrin for fast recombination to the sensitizer cation. The fast recombination rate can be rationalized as a result of the greater electronic coupling to the conduction band. This demonstrates the importance of anchoring groups as a way of mitigating recombination in a porphyrin-sensitized solar cell. This ease of recombination may be exacerbated by axial-bound porphyrins, which have been shown to perform less favorably than *meso*-bound porphyrins.^{10,15,49} In contrast, PPor-OPh-AcAc and PPor-OPh-COO[−] have different charge injection kinetics, with similar mechanisms of charge recombination giving similar *J*-*V* characteristics.

4. Photooxidation of Ir(III)Cp*

Our measurements of TRTS, solar cell performance, and quantum dynamics simulations show that photoinduced electron injection occurs from the excited states of PPor into the semiconductor conduction band. Such an interfacial electron transfer (IET) process oxidizes the porphyrin, generating a strong oxidant intermediate that can be used for water-oxidation. Here, we explore whether PPor can advance the oxidation state of the water-oxidation pre-catalyst Ir(III)Cp*.^{29–31} This complex is synthetically accessible and undergoes redox state transitions (*e.g.*, Ir(III) to Ir(IV)) that can be probed by well-known spectroscopic features.⁵⁰ In addition, its photocurrent properties have been studied.¹² However, PPor sensitizers capable of photooxidizing IrCp* on the metal oxide surface have not yet been reported. Here, we use electron paramagnetic resonance (EPR) spectroscopy to demonstrate the photooxidation of IrCp* by PPor covalently bound to the SnO_2 surface.

4.1 Steady-state fluorescence studies

We first investigated whether the steady-state fluorescence of the PPor and the precatalyst in solution showed any evidence of electron transfer (ESI, Fig. S12† shows a series of fluorescence spectra for various PPor in the presence and absence of the IrCp* precatalyst). The experiments were carried out at the same concentration of porphyrin for all samples. The spectra were measured with an excitation wavelength of 550 nm, which excites the Q-band transition of the porphyrin. Fig. S12a† shows a comparison of the fluorescence spectra of PPor-OPh-COOH, PPor-OPh-AcAcH and their reference compound PPor-OMe (ESI, Scheme S1†) in acetonitrile. The fluorescence intensities of the three porphyrins are virtually identical indicating that the presence of the axially bound anchoring group has no significant effect on the excited state lifetime or fluorescence quantum yield. Similarly, no change in fluorescence is observed when the IrCp*-COOH precatalyst is added to a solution of PPor-OMe or PPor-OPh-AcAcH (ESI, Fig. S12b and S12d†). In contrast,

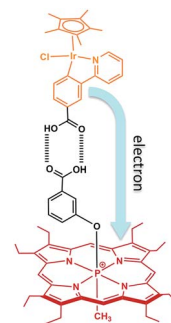


Fig. 7 Proposed electron transfer in the heterodimer (PPor-OPh-COOH...:HOOC-IrCp*) complex.

significant quenching of the fluorescence occurs when the precatalyst is mixed with PPor-OPh-COOH in acetonitrile solution (ESI, Fig. S12c†). Similar results were obtained when PPor-OPh-COOH was titrated with IrCp*-COOH in acetonitrile (ESI, Fig. S13†). We postulate that quenching occurs in the heterodimeric complex (PPor-OPh-COOH...:HOOC-IrCp*, Fig. 7) which is formed as a result of hydrogen bonding between carboxylic acid groups of IrCp*-COOH and PPor-OPh-COOH.⁵¹ The formation of the heterodimeric complex is a competitive process because homodimeric complexes PPor-OPh-COOH...:HOOC-PhO-PPor and IrCp*-COOH...:HOOC-IrCp* can also be formed. If we assume that the equilibrium constants for the formation of the three complexes are the same, then at most one third of the porphyrin molecules will be in the PPor-OPh-COOH...:HOOC-IrCp* complex. Thus, the fact that roughly one third of the fluorescence is quenched (ESI, Fig. S12c†) implies essentially complete quenching in the complex. Based on the redox properties of PPor-OPh-COOH and IrCp*-COOH, this quenching could be caused by electron transfer from IrCp* to the excited porphyrin, which has a driving force of about -0.51 eV (Fig. 2). A similar electron transfer has been observed in a number of donor-acceptor systems with hydrogen bonding between two carboxylic acid groups bridging the electron donor and acceptor parts of the system.^{52,53} Although we cannot exclude the possibility that the quenching is due to the heavy atom effect of Ir, that mechanism is unlikely due to the relatively large distance between the porphyrin and the metal center. Overall these results suggest that PPor could be suitable for advancing the oxidation state of Ir^{III}Cp* as required for catalytic water oxidation.

4.2 Electron paramagnetic resonance spectroscopy

The fluorescence studies suggest that PPor-OPh-COOH is able to photo-oxidize IrCp*-COOH when the two compounds form an H-bonded complex. However, our goal is to achieve this when the two species are co-deposited on the photoanode surface, as illustrated in Fig. 1. Therefore, we tested whether such an activation mechanism is feasible through EPR measurements of the two species bound to SnO_2 nanoparticles. Samples of PPor-OPh-COOH only, or PPor-OPh-COOH and IrCp*-COOH co-deposited on SnO_2 nanoparticles were prepared (see Section 3.2 for details) and then cooled to 80 K and irradiated with continuous white

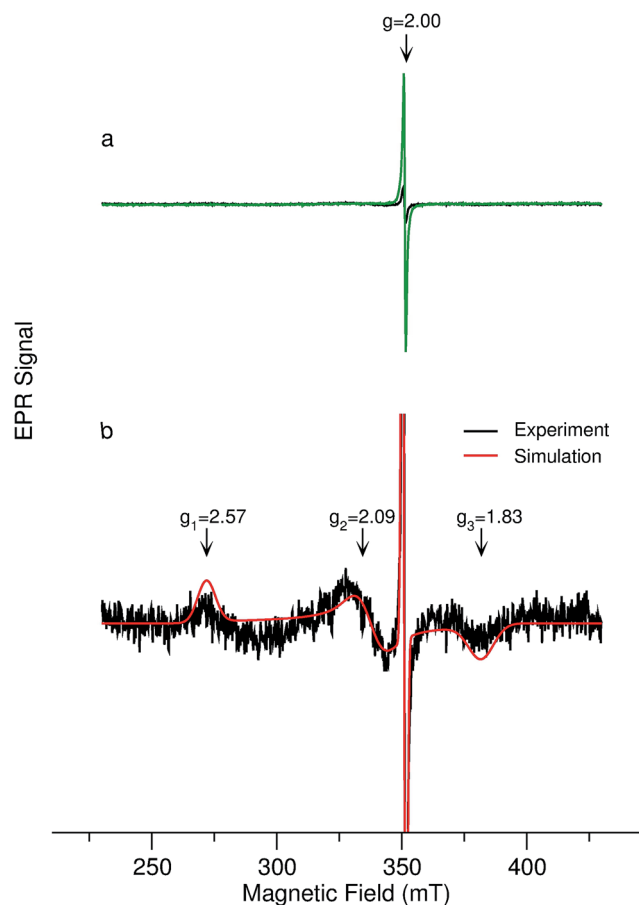


Fig. 8 CW EPR spectrum of PPor and IrCp* co-anchored SnO₂ nanoparticles in presence of white light at 80 K with dark spectrum subtracted. (a) Comparison of SnO₂ nanoparticles with PPor-OPh-COO⁻ (green spectrum) and with PPor-OPh-COOH + IrCp*-COO⁻ (black spectrum). (b) Expanded view of the spectrum of SnO₂ nanoparticles with PPor-OPh-COO⁻ + IrCp*-COO⁻ (black) and its simulation (red). The simulation is the sum of an Ir(IV) species with a rhombic *g*-tensor and a porphyrin radical with an isotropic *g*-tensor. The principal values of the Ir(IV) *g*-tensor in the simulation were *g*₁ = 2.57, *g*₂ = 2.09, *g*₃ = 1.83 and an inhomogeneous broadening of 300 MHz was used. The porphyrin radical was simulated with a *g*-value of 2.00 and an inhomogeneous linewidth of 40 MHz.

light. Fig. 8 shows the difference of spectra, collected in the dark and under illumination, revealing the light-induced EPR signals. Irradiation of the PPor-OPh-COO⁻/SnO₂ samples results in a strong light-induced signal at *g* = 2.00 which is typical of an organic radical (Fig. 8a, green spectrum). This signal is only observed when PPor is bound to the SnO₂ and is probably due to oxidized PPor. A contribution from free electrons in the conduction band is also possible. The intensity of this signal is greatly reduced when IrCp*-COO⁻ is also bound to the SnO₂ nanoparticles (Fig. 8a, black spectrum), while a rhombic EPR spectrum with principal *g*-values of *g*₁ = 2.57, *g*₂ = 2.09 and *g*₃ = 1.83 emerges (Fig. 8b). The rhombic spectrum is not present when only PPor-OPh-COO⁻ is bound to SnO₂ and none of the signals is observed if only IrCp*-COO⁻ is bound to the nanoparticles (data not shown). The *g*-values of the rhombic spectrum are typical of a transition metal ion and are very similar to those

recently reported for Ir(IV) in a closely related complex;⁵⁰ thus, we assign it to photo-oxidized IrCp*. The contribution from Ir(IV) appears weaker than that of the porphyrin because it is much broader, as a result of the stronger spin-orbit coupling in the metal. However, the simulation (Fig. 8b, red spectrum) reveals that the Ir(IV) contribution corresponds to ~40 times as many spins as the porphyrin radical. This implies efficient electron transfer, as required to achieve light-induced oxidation of a water-splitting with a photoactivated IrCp* catalyst co-deposited with a photosensitizer on a semiconductor anode. The electron-transfer mechanism, depicted in Fig. 1, between the three redox-active units PPor, IrCp* and SnO₂, is thus consistent with the EPR data. Upon irradiation of the PPor at 80 K, an electron is injected into the conduction band of SnO₂ from the excited state of PPor. This is followed by electron transfer to the oxidized porphyrin from a nearby IrCp* molecule. Charge recombination then occurs by back electron transfer to IrCp* from SnO₂ either directly or *via* the porphyrin. In the absence of IrCp*, only the first electron-transfer step occurs. Consequently, when only PPor-OPh-COO⁻ is bound to the SnO₂, the porphyrin radical cation is observed in the EPR spectrum. In the presence of IrCp*, the signal from the porphyrin radical cation is diminished and while the spectrum of Ir(IV) due to the oxidized IrCp* appears.

4.3 Photocurrent studies

We measured the time dependence of the photocurrent in photoelectrochemical cells with (PPor-OPh-COO⁻ + IrCp*-COO⁻)/SnO₂, PPor-OPh-COO⁻/SnO₂, IrCp*-COO⁻/SnO₂ and bare SnO₂ as the anodes. The cells were illuminated for about 10 min with alternating light and dark periods of 100 s. Fig. 9 shows plots of the photocurrent *versus* time for this illumination procedure. As expected, negligible photocurrent was generated with anodes composed of IrCp*-COO⁻/SnO₂ or bare SnO₂ (Fig. 9, orange and black trace, respectively), while strong photocurrent signals due to electron injection from PPor to the conduction band of SnO₂ were observed with PPor-OPh-COO⁻/

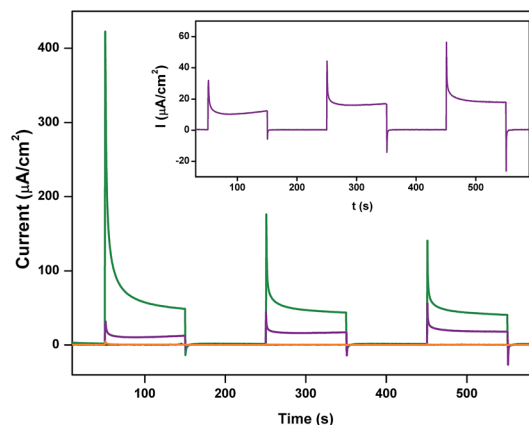


Fig. 9 Photocurrent measurements of SnO₂ (black), IrCp*-COO⁻/SnO₂ (orange), (PPor-OPh-COO⁻)/SnO₂ (green), and (PPor-OPh-COO⁻ + IrCp*-COO⁻)/SnO₂ (purple) photoanodes. Inset shows photocurrent from (PPor-OPh-COO⁻ + IrCp*-COO⁻)/SnO₂ photoanode.

SnO₂ (green trace) and (PPor-OPh-COO⁻ + IrCp^{*}-COO⁻)/SnO₂ (purple trace). A sharp spike as a result of charging of the capacitance of the cell appears at the beginning of each illumination period. The current then decays to a steady-state level and a negative discharging current spike is observed when the light is turned off. With only PPor bound (green trace), a larger current is observed than with PPor and IrCp^{*} (purple trace) because of the higher concentration of sensitizer on the SnO₂ electrode. In addition to the different current magnitudes, the behavior of these two systems over successive illumination periods is also different. In the case of PPor-OPh-COO⁻/SnO₂, the initial charging current is large compared to the steady-state current in the first illumination but drops significantly in each successive illumination, while the steady-state current remains constant. This implies that a significant surface charge, probably due to the PPor⁺, builds up on the anode and that the majority of this charge dissipates on a time scale much longer than 100 s when the light is turned off.

In contrast to the photocurrents obtained for PPor-OPh-COO⁻/SnO₂, anodes with co-deposited PPor-OPh-COO⁻ and IrCp^{*}-COO⁻ showed an increase of both the charging current and the steady-state current with repeated illumination (Fig. 9, inset). These results suggest that the presence of IrCp^{*} introduces alternative electron-transfer pathways.¹⁰ Possible pathways are quenching of the PPor excited state by rapid, reversible electron transfer from IrCp^{*} to PPor, or rapid charge recombination between the injected electron and the oxidized IrCp^{*}. Both of these processes would diminish with prolonged illumination and accumulation of oxidized IrCp^{*} on the electrode surface, leading to both greater steady-state current as observed. The EPR measurements support the hypothesis that the increased current is due to build-up of Ir(IV) centers on the SnO₂ surface. The increased spin population, relative to PPor radicals, indicates that injection from PPor into the SnO₂ conduction band is rapid, as is reductive electron transfer from IrCp^{*} to PPor. By contrast, reduction of Ir(IV) by recombination from conduction band electrons is comparatively slow, allowing for accumulation of oxidized IrCp^{*} on the SnO₂ surface.

5. Conclusions and outlook

We have shown that phosphorus(v) porphyrins (PPors) are effective photosensitizers for photocatalytic solar cells, when covalently bound to SnO₂ surfaces. Upon photoexcitation with visible light, they generate anodic potentials in the 1.62–1.65 V (vs. NHE) range, sufficiently positive as to activate a well-known water oxidation pre-catalyst (IrCp^{*}). The oxidation state of IrCp^{*} is advanced by photoexcitation of PPors, even when the IrCp^{*} and the PPor are not covalently bound with each other, as long as they are co-deposited on the same SnO₂ surface. The co-deposition strategy bypasses the synthetic challenge of covalently linking the chromophore to the catalyst.^{32,33} Codeposition also suppresses the possibility of quenching the photoexcitation of the PPor chromophore by direct interaction with the heavy-atom catalytic metal center. A similar co-deposition strategy has been previously attempted in studies of pentafluorophenylzinc(II) porphyrin deposited on TiO₂,¹² although

oxidation of the co-deposited IrCp^{*} could only be inferred from changes in the TRTS data. Here, we find for the first time direct evidence of photooxidation of IrCp^{*} by PPor on the SnO₂ surface. Our results demonstrate that co-deposition of PPor and IrCp^{*} on SnO₂ provides high-potential photoanodes as required for water oxidation. At the same time, our analysis shows that additional work is needed to optimize the electron-transfer process as required for water oxidation. The computations show that the explored anchoring groups, including *m*-hydroxidebenzoate (⁻OPh-COO⁻) and 3-(3-phenoxy)-acetylacetonate (⁻OPh-AcAc) are less than optimal for charge separation since they do not couple enough with orbitals in the porphyrin, leading to slower injection from the PPor than from the linker. TRTS shows that the injection efficiencies follow the trend PPor-O⁻ > PPor-OPh-COO⁻ > PPor-OPh-AcAc, while solar cell efficiencies follow the opposite order: PPor-O⁻ < PPor-OPh-COO⁻ ≈ PPor-OPh-AcAc. These results indicate that there is a subtle balance between electron injection and recombination, as a function of distance and orientation of the porphyrin with respect to the semiconductor surface. Further optimization should aim at increasing the electron donor character to help vector the electron into the conduction band while avoiding recombination from the SnO₂ surface.

Acknowledgements

This work was supported by the Natural Science and Engineering Research Council of Canada in the form of a Discovery Grant (AvdE, P.P.K.), the U.S. Department of Energy Office of Basic Sciences DE-FG02-07ER15909 (J.M.T., R.L.M., S.W.S., C.A.S., G.W.B.), and the National Science Foundation DGE-1122492 (S.W.S.). Computational work was supported as part of the Argonne-Northwestern Solar Energy Research (ANSER) Center, an Energy Frontier Research Center funded by the U.S. Department of Energy, Office of Science, Office of Basic Energy Sciences under Award Number DE-SC0001059 (V.S.B.). We thank Prof. Robert H. Crabtree (Yale University) for providing the IrCp^{*} water-oxidation precatalyst, Prof. Melanie Pilkington and Prof. Jeffrey Atkinson (Department of Chemistry, Brock University) for the use of their research equipment.

Notes and references

- 1 N. S. Lewis and D. G. Nocera, *Proc. Natl. Acad. Sci. U. S. A.*, 2006, **103**, 15729–15735.
- 2 N. Armaroli and V. Balzani, *Angew. Chem., Int. Ed.*, 2007, **46**, 52–66.
- 3 G. W. Crabtree and N. S. Lewis, *Phys. Today*, 2007, **60**, 37–42.
- 4 D. Gust, T. A. Moore and A. L. Moore, *Acc. Chem. Res.*, 2009, **42**, 1890–1898.
- 5 L. Hammarström and S. Hammes-Schiffer, *Acc. Chem. Res.*, 2009, **42**, 1859–1860.
- 6 A. J. Morris, G. J. Meyer and E. Fujita, *Acc. Chem. Res.*, 2009, **42**, 1983–1994.
- 7 S. C. Roy, O. K. Varghese, M. Paulose and C. A. Grimes, *ACS Nano*, 2010, **4**, 1259–1278.

- 8 G. F. Moore and G. W. Brudvig, in *Annual Review of Condensed Matter Physics*, 2011, vol. 2, pp. 303–327.
- 9 K. J. Young, L. A. Martini, R. L. Milot, R. C. Snoeberger, V. S. Batista, C. A. Schmittenmaer, R. H. Crabtree and G. W. Brudvig, *Coord. Chem. Rev.*, 2012, **256**, 2503–2520.
- 10 G. F. Moore, S. J. Konezny, H. E. Song, R. L. Milot, J. D. Blakemore, M. L. Lee, V. S. Batista, C. A. Schmittenmaer, R. H. Crabtree and G. W. Brudvig, *J. Phys. Chem. C*, 2012, **116**, 4892–4902.
- 11 W. J. Youngblood, S. H. A. Lee, Y. Kobayashi, E. A. Hernandez-Pagan, P. G. Hoertz, T. A. Moore, A. L. Moore, D. Gust and T. E. Mallouk, *J. Am. Chem. Soc.*, 2009, **131**, 926–927.
- 12 G. F. Moore, J. D. Blakemore, R. L. Milot, J. F. Hull, H. E. Song, L. Cai, C. A. Schmittenmaer, R. H. Crabtree and G. W. Brudvig, *Energy Environ. Sci.*, 2011, **4**, 2389–2392.
- 13 Y. X. Zhao, J. R. Swierk, J. D. Megiatto, B. Sherman, W. J. Youngblood, D. D. Qin, D. M. Lentz, A. L. Moore, T. A. Moore, D. Gust and T. E. Mallouk, *Proc. Natl. Acad. Sci. U. S. A.*, 2012, **109**, 15612–15616.
- 14 J. M. Gardner, M. Beyler, M. Karnahl, S. Tschierlei, S. Ott and L. Hammarström, *J. Am. Chem. Soc.*, 2012, **134**, 19322–19325.
- 15 L. A. Martini, G. F. Moore, R. L. Milot, L. Z. Cai, S. W. Sheehan, C. A. Schmittenmaer, G. W. Brudvig and R. H. Crabtree, *J. Phys. Chem. C*, 2013, **117**, 14526–14533.
- 16 Y. Gao, X. Ding, J. H. Liu, L. Wang, Z. K. Lu, L. Li and L. C. Sun, *J. Am. Chem. Soc.*, 2013, **135**, 4219–4222.
- 17 P. P. Kumar, G. Premaladha and B. G. Maiya, *Chem. Commun.*, 2005, 3823–3825.
- 18 Y. E. Kandrashkin, P. K. Poddutoori and A. van der Est, *Appl. Magn. Reson.*, 2006, **30**, 605–618.
- 19 P. K. Poddutoori, A. Dion, S. J. Yang, M. Pilkington, J. D. Wallis and A. van der Est, *J. Porphyrins Phthalocyanines*, 2010, **14**, 178–187.
- 20 P. K. Poddutoori, P. Poddutoori, B. G. Maiya, T. K. Prasad, Y. E. Kandrashkin, S. Vasil'ev, D. Bruce and A. van der Est, *Inorg. Chem.*, 2008, **47**, 7512–7522.
- 21 K. Hirakawa, S. Kawanishi, T. Hirano and H. Segawa, *J. Photochem. Photobiol., B*, 2007, **87**, 209–217.
- 22 C. A. Marrese and C. J. Carrano, *Inorg. Chem.*, 1983, **22**, 1858–1862.
- 23 C. A. Marrese and C. J. Carrano, *J. Chem. Soc., Chem. Commun.*, 1982, 1279–1280.
- 24 L. Giribabu, T. A. Rao and B. G. Maiya, *Inorg. Chem.*, 1999, **38**, 4971–4980.
- 25 H. Segawa, K. Kunitomo, K. Susumu, M. Taniguchi and T. Shimidzu, *J. Am. Chem. Soc.*, 1994, **116**, 11193–11194.
- 26 M. Borgstrom, E. Blart, G. Boschloo, E. Mukhtar, A. Hagfeldt, L. Hammarström and F. Odobel, *J. Phys. Chem. B*, 2005, **109**, 22928–22934.
- 27 K. Y. Akiba, R. Nadano, W. Satoh, Y. Yamamoto, S. Nagase, Z. P. Ou, X. Y. Tan and K. M. Kadish, *Inorg. Chem.*, 2001, **40**, 5553–5567.
- 28 R. L. Milot, G. F. Moore, R. H. Crabtree, G. W. Brudvig and C. A. Schmittenmaer, *J. Phys. Chem. C*, 2013, **117**, 21662–21670.
- 29 J. F. Hull, D. Balcells, J. D. Blakemore, C. D. Incarvito, O. Eisenstein, G. W. Brudvig and R. H. Crabtree, *J. Am. Chem. Soc.*, 2009, **131**, 8730–8731.
- 30 J. D. Blakemore, N. D. Schley, D. Balcells, J. F. Hull, G. W. Olack, C. D. Incarvito, O. Eisenstein, G. W. Brudvig and R. H. Crabtree, *J. Am. Chem. Soc.*, 2010, **132**, 16017–16029.
- 31 U. Hintermair, S. W. Sheehan, A. R. Parent, D. H. Ess, D. T. Richens, P. H. Vaccaro, G. W. Brudvig and R. H. Crabtree, *J. Am. Chem. Soc.*, 2013, **135**, 10837–10851.
- 32 M. T. Vagnini, A. L. Smeigh, J. D. Blakemore, S. W. Eaton, N. D. Schley, F. D'Souza, R. H. Crabtree, G. W. Brudvig, D. T. Co and M. R. Wasielewski, *Proc. Natl. Acad. Sci. U. S. A.*, 2012, **109**, 15651–15656.
- 33 L. Alibabaei, M. K. Brennaman, M. R. Norris, B. Kalanyan, W. J. Song, M. D. Losego, J. J. Concepcion, R. A. Binstead, G. N. Parsons and T. J. Meyer, *Proc. Natl. Acad. Sci. U. S. A.*, 2013, **110**, 20008–20013.
- 34 J. B. Baxter and C. A. Schmittenmaer, *J. Phys. Chem. B*, 2006, **110**, 25229–25239.
- 35 M. C. Beard, G. M. Turner and C. A. Schmittenmaer, *Phys. Rev. B: Condens. Matter Mater. Phys.*, 2000, **62**, 15764–15777.
- 36 M. C. Beard, G. M. Turner and C. A. Schmittenmaer, *J. Phys. Chem. B*, 2002, **106**, 7146–7159.
- 37 L. G. C. Rego and V. S. Batista, *J. Am. Chem. Soc.*, 2003, **125**, 7989–7997.
- 38 R. C. Snoeberger, T. Lian and V. S. Batista, *The influence of surface hydration on the interfacial electron transfer dynamics from Rhodamine B in SnO₂*, San Diego, CA, 2009.
- 39 M. J. Frisch, G. W. Trucks, H. B. Schlegel, G. E. Scuseria, M. A. Robb, J. R. Cheeseman, G. Scalmani, V. Barone, B. Mennucci, G. A. Petersson, H. Nakatsuji, M. Caricato, X. Li, H. P. Hratchian, A. F. Izmaylov, J. Bloino, G. Zheng, J. L. Sonnenberg, M. Hada, M. Ehara, K. Toyota, R. Fukuda, J. Hasegawa, M. Ishida, T. Nakajima, Y. Honda, O. Kitao, H. Nakai, T. Vreven, J. A. J. Montgomery, J. E. Peralta, F. Ogliaro, M. Bearpark, J. J. Heyd, E. Brothers, K. N. Kudin, V. N. Staroverov, R. Kobayashi, J. Normand, K. Raghavachari, A. Rendell, J. C. Burant, S. S. Iyengar, J. Tomasi, M. Cossi, N. Rega, J. M. Millam, M. Klene, J. E. Knox, J. B. Cross, V. Bakken, C. Adamo, J. Jaramillo, R. Gomperts, R. E. Stratmann, O. Yazyev, A. J. Austin, R. Cammi, C. Pomelli, J. W. Ochterski, R. L. Martin, K. Morokuma, V. G. Zakrzewski, G. A. Voth, P. Salvador, J. J. Dannenberg, S. Dapprich, A. D. Daniels, Ö. Farkas, J. B. Foresman, J. V. Ortiz, J. Cioslowski and D. J. Fox, *Gaussian 09 Gaussian Inc*, Wallingford CT, 2009.
- 40 J. M. Soler, E. Artacho, J. D. Gale, A. Garcia, J. Junquera, P. Ordejon and D. Sanchez-Portal, *J. Phys.: Condens. Matter*, 2002, **14**, 2745–2779.
- 41 Y. Arai and H. Segawa, *Chem. Lett.*, 2013, **42**, 918–920.
- 42 J. Rochford, D. Chu, A. Hagfeldt and E. Galoppini, *J. Am. Chem. Soc.*, 2007, **129**, 4655–4665.
- 43 Y. Mikata, T. Sawaguchi, T. Kakuchi, M. Gottschaldt, U. S. Schubert, H. Ohi and S. Yano, *Eur. J. Org. Chem.*, 2010, 663–671.
- 44 N. W. Ashcroft and N. D. Mermin, *Solid State Physics*, Saunders College, Philadelphia PA, 1976.

- 45 M. Fujitsuka, D. W. Cho, S. Tojo, A. Inoue, T. Shiragami, M. Yasuda and T. Majima, *J. Phys. Chem. A*, 2007, **111**, 10574–10579.
- 46 E. Galoppini, *Coord. Chem. Rev.*, 2004, **248**, 1283–1297.
- 47 C. X. She, J. C. Guo, S. Irle, K. Morokuma, D. L. Mohler, H. Zabri, F. Odobel, K. T. Youm, F. Liu, J. T. Hupp and T. Lian, *J. Phys. Chem. A*, 2007, **111**, 6832–6842.
- 48 O. S. Wenger, *Acc. Chem. Res.*, 2011, **44**, 25–35.
- 49 C. F. A. Negre, R. L. Milot, L. A. Martini, W. Ding, R. H. Crabtree, C. A. Schmuttenmaer and V. S. Batista, *J. Phys. Chem. C*, 2013, **117**, 24462–24470.
- 50 T. P. Brewster, J. D. Blakemore, N. D. Schley, C. D. Incarvito, N. Hazari, G. W. Brudvig and R. H. Crabtree, *Organometallics*, 2011, **30**, 965–973.
- 51 Y. Ihaya and T. Shibuya, *Bull. Chem. Soc. Jpn.*, 1965, **38**, 1144–1147.
- 52 C. Turro, C. K. Chang, G. E. Leroi, R. I. Cukier and D. G. Nocera, *J. Am. Chem. Soc.*, 1992, **114**, 4013–4015.
- 53 P. J. F. Derege, S. A. Williams and M. J. Therien, *Science*, 1995, **269**, 1409–1413.
- 54 S. W. Sheehan, H. Noh, G. W. Brudvig, H. Cao and C. A. Schmuttenmaer, *J. Phys. Chem. C*, 2013, **117**, 927–934.